Local nuclear to cytoplasmic ratio regulates chaperone-dependent H3 variant incorporation during zygotic genome activation

Anusha D. Bhatt[1#], Madeleine G. Brown[1#], Aurora B. Wackford[1], Yuki Shindo[1], Amanda A. Amodeo[1,2,*]
[1]Department of Biological Sciences, Dartmouth College, Hanover, NH 03755, USA
[2] Lead contact
[#]Authors contributed equally
*Correspondence: amanda.amodeo@dartmouth.edu

Summary
Early embryos often have relatively unstructured chromatin that lacks active and inactive domains typical of differentiated cells. In many species, these regulatory domains are established during zygotic genome activation (ZGA). In *Drosophila*, ZGA occurs after 13 fast, reductive, syncytial nuclear divisions during which the nuclear to cytoplasmic (N/C) ratio grows exponentially. These divisions incorporate maternally-loaded, cytoplasmic pools of histones into chromatin. Previous work found that chromatin incorporation of replication-coupled histone H3 decreases while its variant H3.3 increases in the cell cycles leading up to ZGA. In other cell types, H3.3 is associated with sites of active transcription as well as heterochromatin, suggesting a link between H3.3 incorporation and ZGA. Here, we examine the factors that contribute to H3.3 incorporation at ZGA. We identify a more rapid decrease in the nuclear availability of H3 than H3.3 over the final pre-ZGA cycles. We also observe an N/C ratio-dependent increase in H3.3 incorporation in mutant embryos with non-uniform local N/C ratios. We find that chaperone binding, not gene expression, controls incorporation patterns using H3/H3.3 chimeric proteins at the endogenous H3.3A locus. We test the specificity of the H3.3 chaperone pathways for H3.3 incorporation using Hira (H3.3 chaperone) mutant embryos. Overall, we propose a model in which local N/C ratios and specific chaperone binding regulate differential incorporation of H3.3 during ZGA.

Keywords: Zygotic genome activation, nuclear to cytoplasmic ratio, histones, chromatin, transcription, heterochromatin

Introduction

Genome accessibility can be dynamically regulated through controlled incorporation of variant histones[1–3]. In most tissues, replication-coupled (RC) histones, produced during S-phase, generate the majority of nucleosomes[2,4,5]. RC histones have unusually high copy number, lack introns, and contain specialized UTRs to facilitate their rapid production during S-phase[3,6–9]. Conversely, replication-independent (RI), "variant" histones are made throughout the cell cycle and incorporated into specific genomic regions[4,10]. The exchange of RC and RI histones on chromatin is a common feature of early embryonic development especially during zygotic genome activation (ZGA) [11–17]. During ZGA, chromatin undergoes extensive remodeling to facilitate bulk transcription and establish heterochromatin[18–25].

Pre-ZGA cells in many organisms depend on maternally supplied components, including histones, as they oscillate between S and M phases without growth phases[26–30]. This leads to an exponential increase in the nuclear to cytoplasmic (N/C) ratio and the rapid consumption of maternal histone stores[29,31–35]. Indeed, the titration of maternal histones against the number of genomes has been proposed to couple cell cycle progression and transcription to the increasing N/C ratio at ZGA[36–43]. Concurrently, histone variants are exchanged on chromatin. Maternally supplied, embryonic-specific linker histone variants are often replaced by RC H1s during ZGA[12–14,16,17]. The RC nucleosomal histone H2A is replaced by RI H2AV due to cell cycle slowing during ZGA in *Drosophila*[15,44]. Similarly, we have previously shown that RC histone H3 is replaced by RI H3.3 during these same cycles, though the cause remains unclear[29].

H3.3 is essential for proper embryonic development in mice, *Xenopus*, and zebrafish[45–49]. In *Xenopus,* the H3.3-specific S31 residue is required for gastrulation while its chaperone binding site is dispensable[48]. In *Drosophila*, H3.3 nulls survive until adulthood using maternal H3.3 but are sterile[50]. Flies expressing H3 from the H3.3 enhancer generated conflicting results as to whether H3.3 protein or simply a source of replication-independent H3 is required for fertility[50,51]. The H3/H3.3 pair is particularly interesting during ZGA because H3.3 is enriched at sites of active transcription and in heterochromatin, which are both established during ZGA[2,4,52].

Here we test the dependence of H3 and H3.3 chromatin incorporation and nuclear accumulation on the local N/C ratio during pre-ZGA cycles in *Drosophila* and identify chaperone binding sites as key regulators of their disparate behaviors. First, we assess how the nuclear availability of H3.3 changes in the pre-ZGA cycles and determine if the local N/C ratios affect H3 versus H3.3 chromatin incorporation. Next, we test if the observed behaviors are due to differences in expression or specific amino acids using chimeric H3/H3.3 histones. Lastly, we assess the role of specific chaperone pathways in the incorporation of these chimeric H3.3 variants in HIRA^{ssm} mutant embryos. Overall, we propose a model where the local N/C ratio and chaperone binding regulate differential incorporation of H3.3 during ZGA.

Results

The interphase nuclear availability of H3 decreases more rapidly than H3.3 over the pre-ZGA cycles

To understand in vivo dynamics of the H3/H3.3 pair during ZGA in *Drosophila*, we have previously tagged H3 and H3.3 with a photo-convertible Dendra2 protein, (H3-Dendra2 and H3.3-Dendra2) at a pseudo-endogenous H3 locus and endogenous H3.3A locus respectively (Figures S1A-B)[29]. *Drosophila* ZGA occurs after 13 rapid syncytial nuclear cycles (NCs) and is accompanied by cell cycle slowing and cellularization. We have previously shown that with each NC, the pool of free H3 is depleted and its levels on chromatin decrease (Figure 1A, S1C)[29]. In contrast, H3.3 chromatin levels increase during the same cycles (Figure 1A, S1C)[29]. To test if changes in the relative nuclear availability of H3 and H3.3 explain the observed chromatin incorporation trends, we measured the nuclear intensities of H3-Dendra2 and H3.3-Dendra2 in each interphase. We observed that H3 nuclear intensities decreased by ~40% between NC10 and NC13 as previously shown (Figure 1B, S1D)[29]. However, when we measured H3.3-Dendra2 nuclear intensities we found that they decreased by only ~20% between NC10 and NC13 (Figure 1B, S1D). To further assess how nuclear uptake dynamics changed during these cycles, we tracked total nuclear H3 and H3.3 in each cycle and found that H3.3 accumulation reduced more slowly than H3 (Figure 1C-D).

The reduction in nuclear accumulation could be due to a decrease in nuclear import, an increase in nuclear export, or both. To test these possibilities, we quantified the rate of nuclear export by photo-converting Dendra2 during interphase and measuring red Dendra2 signal over time. Using this method, we have previously shown that nuclear export of H3 is negligible[29]. Here, we find that export of H3.3 is also negligible (Figure S1E). These data suggest that the distinct dynamics of H3 and H3.3 nuclear availability are due to their import dynamics. Though the change in initial import rates between NC10 and NC13 are similar between the two histones (Figure 1E), we observed a notable difference in their behavior in NC13. H3 nuclear accumulation plateaus ~5 minutes into NC13, whereas H3.3 nuclear accumulation merely slows (Figure 1C-D). These changes in nuclear import and incorporation result in a less dramatic loss of the free nuclear H3.3 pool than previously seen for H3 (Figure 1F)[29]. Overall, this led to the hypothesis that limiting H3 availability in the later nuclear cycles leads to increased H3.3 chromatin incorporation.

H3 and H3.3 chromatin incorporation are dictated by the local N/C ratio

One factor that could limit H3 nuclear availability is the burgeoning N/C ratio. If maternal histones are uniformly distributed in the early embryonic cytoplasm, the amount of histone available for nuclear uptake would depend on the number of nuclei within the radius of diffusion. This might limit the H3 pool available for chromatin incorporation at high N/C ratios. To test whether the local N/C ratio determines histone chromatin incorporation within a nuclear cycle, we employed our Dendra2-tagged histones in Shackleton (Shkl) embryos which have non-uniform local nuclear densities across the anterior/posterior axis (Figure 2A-B)[53]. Impaired cortical migration of early nuclei increases the N/C ratio in the center and decreases it in the posterior, where it results in frequent partial extra divisions[53]. For our analyses, we manually defined low and high nuclear density regions, with the low-density region always undergoing an extra division (Figure 2B, see

methods). To control for potential positional effects, we measured chromatin incorporation at the middle and pole regions of control embryos for comparison (Figure 2A). In control embryos, the drop in the total amount of H3 and rise in total H3.3 on chromatin are comparable between the middle and pole regions over the pre-ZGA cycles (Figure 2C-D). In contrast, in Shkl embryos, we observe decreased incorporation of H3 on chromatin at high nuclear densities compared to that at low densities, consistent with a model in which H3 becomes limiting at high N/C ratios (Figure 2E). This trend is reversed for H3.3, where chromatin from high densities has more total H3.3 than chromatin from low densities (Figure 2F). This observation indicates that incorporation of H3 and H3.3 are reciprocal and depend, at least in part, on the local N/C ratio.

H3 and H3.3 nuclear imports are sensitive to the local N/C ratio to different extents

To ask whether nuclear availability can explain the N/C ratio-dependent differences in H3 and H3.3 incorporation, we measured their interphase accumulation in Shkl embryos. Since H3 and H3.3 both have negligible nuclear export, their nuclear availabilities are determined by their import rates (Figure S1A)[29]. To assess the impact of the N/C ratio on nuclear import in individual nuclei, we calculated the number of neighbors within a 20 μm radius for each nucleus at its minimum volume (Figure 2G, Figure S2A). We then binned the nuclei by their number of neighbors and determined their nuclear import curves for both H3 and H3.3. In control NC13 embryos, there is little variation in the number of neighbors and all nuclei import H3 and H3.3 similarly (Figure 2H, I, L, and M). In NC13 Shkl embryos, H3 import is anticorrelated with the local N/C ratio. We observed slower H3 nuclear uptake at high N/C ratios resulting in lower total interphase H3 accumulation (Figure 2J). This was also reflected in the initial H3 import rates where the nuclei with fewer neighbors had higher slopes (Figure 2N). H3.3 uptake was less affected by the local N/C ratio. Though H3.3 import was slower in nuclei with more neighbors, the effect was not as dramatic as seen for H3 (Figure 2K-O). A similar trend was also observed in NC12 for both histones, where more neighbors correspond to slower import. However, the range of behaviors was not as large as seen in NC13 (Figure S2F-G). These observations support a model where H3 pools are exhausted by the increasing N/C ratio, increasing the relative availability of H3.3 to H3 over the pre-ZGA cycles.

Chaperone binding sites regulate the differences in H3 and H3.3 chromatin incorporation

We next investigated what differences between H3 and H3.3 caused the observed trends in chromatin incorporation. There are two major differences between H3 and H3.3: protein sequence and expression pattern. H3 differs from H3.3 by four amino acids which create an additional phosphosite in H3.3 and generate differing affinities for specific H3-family histone chaperones[54]. H3 is also generally expressed at much higher levels and in a replication-dependent manner. To determine which factor controls nuclear availability and chromatin incorporation, we genetically engineered flies to express Dendra2-tagged H3/H3.3 chimeras at the endogenous H3.3A locus. These chimeras include (i) H3.3's phosphosite replaced with Alanine from H3 ($H3.3^{S31A}$) (ii) H3.3's chaperone binding domain replaced with H3's ($H3.3^{SVM}$), and (iii) all four H3.3-specific amino acids replaced with those of H3 ($H3.3^{ASVM}$), (Figure 3A). In all cases, the gene structure, including the promoter, intron, and UTRs of H3.3, remained intact and no other codons were changed to maximize similarity to the endogenous H3.3A locus.

To study how chromatin incorporation differed in these chimeras, we measured their total intensities on mitotic chromatin during each nuclear cycle. We observed that, though H3.3^{S31A} chromatin incorporation was significantly reduced compared to H3.3 by NC13, its levels increased on chromatin over the nuclear cycles, resembling H3.3 more than H3 (Figure 3B, S3A). Conversely, the total amount of H3.3^{SVM} and H3.3^{ASVM} on mitotic chromatin fell over the nuclear cycles, similar to H3 (Figure 3B, S3B-C). This suggests that chromatin incorporation is mainly determined by the chaperone binding site. These results are broadly consistent with the final interphase nuclear concentrations where the drop in H3.3^{S31A} was intermediate between H3 and H3.3 while H3.3^{ASVM} was similar to H3 and H3.3^{SVM} fell even faster than H3 (Figure 3C, S3A-C). The differences in interphase nuclear accumulation appear to be due primarily to changes in import in the later half of NC13 (Figure 3D-G). Although there is little difference in the change in the initial nuclear import rate of the chimeras (Figure 3G), H3.3^{SVM} and H3.3^{ASVM} nuclear accumulation plateaus around 5 minutes into NC13 (Figure 3E-F). This was not the case for H3.3^{S31A} where import merely slows in the second half of NC13 as seen in H3.3 (Figure 1F and 3D). However, the lower import of H3.3^{S31A} and H3.3^{SVM} compared to wildtype H3.3 and H3 respectively suggests the possibility that histones with mismatched sites may result in generally reduced nuclear import. Nonetheless, these data indicate that the specific amino acid sequence of the chaperone binding site is the primary factor in differentiating the two histones for chromatin incorporation and nuclear import dynamics.

H3 chaperone binding site conveys independence from Hira for chromatin incorporation

Since the chromatin incorporation of the H3/H3.3 chimeras appears to depend on their chaperone binding sites, we asked whether they still required the canonical H3.3 chaperone, Hira. We used Hira$^{ssm-185b}$ (hereafter Hira^{ssm}) flies which have a point mutation in the Hira locus[55]. The resulting protein can bind but not incorporate H3.3 into chromatin, resulting in sperm chromatin decondensation defects. These embryos develop as haploids and undergo one additional syncytial division before ZGA (NC14)[55]. Though incapable of Hira-dependent chromatin incorporation, the Hira^{ssm} flies import H3.3 into the nucleus (Figure 4A, 4B, S4A). H3 import and incorporation were less affected by the Hira^{ssm} mutation (Figure 4C-D, S4B). The decrease in H3 interphase nuclear concentration by the end of NC14 is comparable to the observed decrease in wildtype embryos by the end of NC13 (Figure 1B and 4D). Similarly, H3 incorporation into chromatin falls by the same amount between NC10 and the end of NC14 as we observed between NC10 and NC13 in wildtype in contrast to our previous findings (Figure 1A and 4C)[29].

To test if H3/H3.3 chimeras use the canonical Hira pathway, we measured import and chromatin incorporation of H3.3^{ASVM} in Hira^{ssm}. We found that H3.3^{ASVM} interphase nuclear concentration was more stable than H3 or H3.3 in the Hira^{ssm} embryos (Figure 4F, S4C). This stability is reflected in H3.3^{ASVM} chromatin incorporation where it only drops by ~20% between NC10 and NC14 compared to the observed ~40% drop in H3 (Figure 4E). These data indicate that H3.3^{ASVM} chromatin incorporation is Hira independent, though expressed from the H3.3A locus. However, the increased relative stability of H3.3^{ASVM} nuclear concentration and chromatin incorporation may

indicate additional regulatory feedback in Hira^{ssm} mutants to maintain chromatin integrity in the absence of H3.3 incorporation.

Discussion

Variant histone switching during ZGA and associated chromatin remodeling marks a critical milestone in development. Here, we sought to understand the factors that dictate incorporation dynamics of the histone-variant pair, H3/H3.3. We found that the relative ratio of H3.3 to H3 nuclear concentrations increased over the pre-ZGA cycles and that their chromatin incorporation was determined by the local N/C ratio. This suggests a model where exhaustion of maternally provided H3 pools leads to H3.3 incorporation. However, our data from the H3/H3.3 chimeras indicate that histone expression levels alone do not dictate incorporation patterns. Rather, their specific chaperone binding sites determine the incorporation dynamics. Overall, our study identifies the local N/C ratio and chaperone binding sites as key determinants of variant histone H3.3 incorporation during ZGA.

Multiple mechanisms may couple H3.3 incorporation to the N/C ratio in a developing embryo. Increasing N/C ratios exhaust maternal pools of H3 which could reduce chromatin incorporation[29,36–38]. Since we observed that H3.3 nuclear accumulation is more stable than H3 as the N/C ratio increases, the relative availability of H3.3 to H3 will increase with the N/C ratio. The precise pathways by which H3.3 is then preferentially incorporated at higher N/C ratios remain unclear. One possibility is that H3.3 is incorporated in conjunction with DNA replication. It has been reported in mammalian cells that when H3 cannot be incorporated through its replication-dependent chaperone CAF-1, Hira can incorporate H3.3 onto newly replicated DNA[56]. Another possibility is that H3.3 incorporation occurs as an indirect effect of increased cell cycle duration. Here the increasing N/C ratio results in a longer interphase duration, allowing a greater window for transcription and heterochromatin formation which recruits H3.3[21,50,57,58]. These possibilities are not mutually exclusive (Figure 4G). Future experiments will be required to disentangle the direct and indirect effects of the N/C ratio on H3.3 incorporation.

H3 nuclear concentration has also been proposed to directly regulate cell cycle length through H3 interactions with Chk1[38]. In Hira^{ssm} embryos that undergo one extra division before cell cycle slowing, the fall in nuclear H3 concentration between NC10 and the final fast cell cycle is strikingly similar to that seen in wildtype. Moreover, H3 nuclear concentrations appear to be strongly sensitive to the local N/C ratio in Shkl embryos. Together these data are consistent with a model in which H3 nuclear concentrations regulate cell cycle slowing. However, H3.3 nuclear concentrations are less sensitive to the local N/C ratio than H3. Since H3.3 has more Chk1 phosphorylation sites than H3 it would be predicted to be a stronger Chk1 regulator[48,59]. The relative contributions of both H3 and H3.3 nuclear availability to cell cycle slowing will require further exploration.

Acknowledgements

We thank Shruthi Balachandra, Eric Alpert, Grace Carey and Kiera Schwarz for constructive discussion of this manuscript. We further thank the members of Bickel, Kasper, Lacefield, Moseley and Landino labs at Dartmouth for their helpful suggestions. We thank Patrick Robison

from the Dartmouth bioMT Core, Ann Lavanway and Britton Johnson for technical support. We thank Stefano Di Talia for shkl stock flies, Eric Weishcaus for ssm stock flies; Robert Marmion for the nos-PBac transposase flies and Robert Duronio for the 1xHisC plasmid. This work was funded by NIH/NIGMS (P20-GM113132 and R35GM150853 to AAA). ADB is supported by Sondra and Charles Gilman Graduate Research Fellowship.

Author contributions

Conceptualization, ADB, MGB, YS and AAA.; Investigation and Analysis, ADB, MGB and ABW; Writing – Original Draft, ADB, MGB and AAA; Writing – Review & Editing, ADB, MGB, YS and AAA.

Materials and methods

Drosophila stocks and genetic crosses

A) y,w; 1xHisC.H3-Dendra2;
B) y,w; H3.3A-Dendra2/CyO;
C) y,w; IX HisC.H3-Dendra2; *shkl*^{GM163}/TM3
D) y,w; IX HisC.H3-Dendra2; *shkl*^{GM130}/TM3
E) y,w; H3.3A-Dendra2/CyO; *shkl*^{GM163}/TM6B
F) y,w; H3.3A-Dendra2/CyO; *shkl*^{GM130}/TM6B
G) y,w; H3.3A-Dendra2^{S31A}/CyO;
H) y,w; H3.3A-Dendra2^{SVM}/CyO;
I) y,w; H3.3A-Dendra2^{ASVM}/CyO;
J) *ssm*^{185b},w/FM7c,*w*^{a}; IX HisC.H3-Dendra2;
K) *ssm*^{185b},w/FM7c,*w*^{a}; H3.3A-Dendra2/CyO;
L) *ssm*^{185b},w/FM7c,*w*^{a}; H3.3A-Dendra2^{S31A}/CyO;
M) *ssm*^{185b},w/FM7c,*w*^{a}; H3.3A-Dendra2^{SVM}/CyO;
N) *ssm*^{185b},w/FM7c,*w*^{a}; H3.3A-Dendra2^{ASVM}/CyO;

Fly stocks A, B, J, and K were generated previously in our lab and are described in Shindo and Amodeo (2019). The Shkl lines y,w; Sp/CyO; *shkl*^{GM163}/TM3 and y,w; Sp/CyO; *shkl*^{GM130}/TM3 were a generous gift from Stefano Di Talia, Duke University. Stocks C, D, E, and F were generated in the lab by the genetic crossing of these Shkl lines with lines A and B. Stocks L, M, and N were generated by crossing the stocks G, H and I with *ssm*^{185b},w/FM7c,*w*^{a};; (a generous gift from Eric Weischaus).

Drosophila husbandry

All fly stocks were maintained at room temperature, on standard molasses media. The egg lay cages were set up to collect embryos at 25°C. Embryos from these cages were collected on apple juice agar plates with yeast paste, dechorionated with 50% bleach for up to 2 minutes (2 min control, 1.25 min H3 shkl, 45 s H3.3 shkl), and washed twice with dH_2O. For shkl embryos, the 2 shkl lines were crossed to obtain *shkl*^{GM130e}/*shkl*^{GM163e} transheterozygous females and their embryos were imaged. The *ssm*^{185b} embryos were collected from *ssm*^{185b}/*ssm*^{185b} homozygous females.

Plasmids and transgenesis

To generate stocks G, H, and I, CRISPR-Cas9 editing was performed at the endogenous H3.3A locus. To this end, pScarlessHD-H3.3A-Dendra2-DsRed plasmid, reported in Shindo and Amodeo (2019) was modified through site-directed mutagenesis to express H3.3 with H3-specific amino acids, generating pScarlessHD-H3.3A^{S31A}-Dendra2-DsRed (S31A mutation), pScarlessHD-H3.3A^{SVM}-Dendra2-DsRed (A87S, I89V, G90M mutations) and pScarlessHD-H3.3A^{ASVM}-Dendra2-DsRed (S31A, A87S, I89V, G90M mutations) plasmids (Genscript). Two CRISPR target sites were identified using Target Finder[60], one near the stop codon and one near S31, and the corresponding gRNAs were cloned into pU6-BbsI-chiRNA vector (a gift from Melissa Harrison & Kate O'Connor-Giles & Jill Wildonger, Addgene plasmid #45946). Each mutant plasmid was co-injected with both the gRNA plasmids into nos-Cas9 embryos (TH00787.N) and DsRed+ progeny were selected (BestGene). These progeny were then crossed with nos-PBac flies(a generous gift from Robert Marmion and Stas Shvartsman) to remove the DsRed marker. DsRed negative single males were then crossed with y,w;Sp/CyO; to establish stocks G, H, and I. Insertion of Dendra2 tagged mutants was verified by PCR and Sanger sequencing.

Microscopy

For live imaging, dechorionated embryos were mounted on glass-bottom MatTek dishes in deionized water and imaged with the 20x, 0.8 NA, objective of Zeiss LSM980 confocal microscope with Airyscan-2 at 45 s intervals for 2 h at room temperature (19-22°C). All H3-Dendra2 tagged embryos were imaged using a 488 nm laser at 2% power and all lines expressing Dendra2 tagged proteins from the endogenous H3.3A locus (H3.3 and the chimeras) were imaged with a 488 nm with 0.5% power in Airyscan multiplex CO-8Y mode. All but shkl embryos and their controls were imaged at a 700 x 700 pixels resolution, with 1 µm Z-steps over a 15 µm range, with a frame time of 26.06ms. All Shkl embryos and their controls (Figure 2) were imaged at a 2836 x 2836 pixels resolution, with 1.2 µm Z-steps over a 14.4 µm range, with a frame time of 328.29ms. All images were acquired with a pixel size of 0.149 µm x 0.149 µm.

Nuclear export and unbound H3.3 measurement through Dendra2 photoconversion

For measuring the nuclear export and amount of free histone H3.3 (Figure 1F and S1E), we used the photoconvertible Dendra2 tag and the interactive bleaching panel in Zen software. We used a 4µm diameter circular stencil to interactively photo-convert the nuclei. H3.3-Dendra2 within a single nucleus was photoconverted from green to red using a 405 nm laser at 3% power with 60 iterations of laser exposure at a speed of 1.37µs/pixel. The nucleus was converted in the middle of each nuclear cycle for NC11-13 and then imaged with 561 nm at 1% laser power and 488 nm with 0.5% laser power at 15-second intervals until the end of the nuclear cycle. Images were captured at 576 x 576 pixels resolution with 1 µm Z-steps over a 15 µm range, with a frame time of 66.55ms for each channel. The images were acquired with a 40x oil immersion objective, 1.3 NA with a pixel size of 0.092 µm x 0.092 µm.

Photobleaching corrections

To assess the potential effects of fluorophore photobleaching during our image capture, we performed parallel embryo experiments. In these experiments, we identified 2 embryos of the

same age and imaged the interphase nucleus and the metaphase chromatin for both in NC10. Following this, we image only a sub-region of one of the two embryos continuously with our experimental settings described for H3-Dendra2 embryos above until NC13, while keeping the other embryo to develop parallelly without imaging. Once the imaged embryo reached NC13, both the imaged and unimaged parallel embryo were imaged again. We quantified the total nuclear signal from both embryos to evaluate the photobleaching effects. We then compared the continuously imaged section of the embryo, with the area outside the sub-region imaged as well as the unimaged parallel embryo. Using these comparisons, we determined that the effect of photobleaching was minimal and therefore did not apply a numeric photobleaching correction to our data (Figure S1F-G, Table S1-2).

Nuclear segmentation and intensity analysis

All raw CZI output files from ZEN 3.3 (blue edition) live imaging were first 3D Airyscan Processed at a strength of 3.7 and then converted into individual TIFF files.

For mitotic chromatin quantification, the time points corresponding to metaphase chromatin from each nuclear cycle were extracted and the z-stacks were sum projected in FIJI (2.14.0/1.54f) These files were segmented using the 'pixel classification + object classification' applet in the ilastik-1.4.0 software[61] into chromatin and cytoplasm. The individually segmented mitotic chromatin objects were then exported as a single CSV file containing object properties such as total intensity, mean intensity, and size. The total intensity within each chromatin mass was calculated and normalized to the average NC10 chromatin values (or NC11 for shkl embryos and their controls) for that genotype.

In Shkl embryos and their controls (Figure 2C-F, S2A-B), chromatin was segmented from different regions within an embryo (middle and pole regions for control, and from low and high-density regions for Shkl). In control embryos, middle regions were defined by outlining a box (250x250 pixels) in NC10 around the line separating the embryo into 2 halves. A similar-sized box was outlined with one edge at the tip of the embryo to define the pole region. In shkl embryos, the regions with the highest apparent nuclear density within the center was defined as the high-density region and the region that underwent the partial extra division in NC14 was defined as the low-density region. To account for the asynchronous nature of the divisions in the shkl embryo, within each region, 5-6 nuclei that divided synchronously along the mitotic wave were quantified. For both control and shkl embryos, at least 5 nuclei per embryo were quantified in each cycle for each region.

For analyzing the interphase nuclear concentrations, nuclei from 45 seconds before the nuclear envelope breakdown were segmented in 3D using the 'pixel classification + object classification' applet on ilastik software. The CSV file with the mean intensities of each nucleus was exported and normalized to the average NC10 nuclear concentration values for each genotype.

For obtaining the nuclear import curves, individual nuclear cycles were run through the pixel classification + object classification applet in the ilastik software. The results were exported as

CSV files and processed with a custom R script. For Shkl embryos (Figure 2H-K), the pixel prediction maps were used with the 'tracking with learning' applet (ilastik) to segment the nuclei as well as track them over time. The tracking result with object properties was exported as a CSV file and processed with a custom R script. Intensities were normalized by the average total intensity of the nuclei at their maximum size in each cycle. For each case, the volume was calculated by multiplying the voxel size with the 'size in pixels' of an object.

Neighborhood analysis

Nuclei within each embryo were tracked over a single nuclear cycle using the 'tracking + learning' applet on ilastik. The tracking result with the coordinates of each nucleus over time was obtained as a CSV file, along with other parameters including the total intensity, mean intensity, and nuclear size. The CSV file was analyzed to calculate the number of nuclear neighbors for each nucleus within a 20 μm radius using a custom R script. The script calculates the number of neighbors each nucleus has at its minimum volume since the maximum nuclear import occurs at this time point. To overcome the noise from the incomplete edge nuclei, which are centered lower in the embryo, we utilized the differences in their Z-coordinates to filter them out, after using them for the number of neighbor calculations. For Shkl embryos, as the nuclear cycles are asynchronous, the total intensity traces were aligned to match their minimum volumes to T0. Nuclei with the same number of neighbors were binned together and weighted to reflect the number of nuclei being averaged. The total intensity curves were then normalized such that the average total intensity of the nuclei at their maximum size was equal to 1.

Statistical analysis

Two-way ANOVA tests were conducted to assess the statistical significance between the dataset means of different genotypes over the nuclear cycles. All studies were performed with multiple nuclei (at least 4 per embryo for NC10, >5 for other cycles) from at least 3 embryos. For Shkl embryos, a two-way ANOVA test was used to determine the statistical significance of nuclei within different regions of the same embryo over the different nuclear cycles. Results from these tests are reported in supplementary tables S1-8.

Figure 1: The interphase nuclear availability of H3 decreases more rapidly than H3.3 over the pre-ZGA cycles

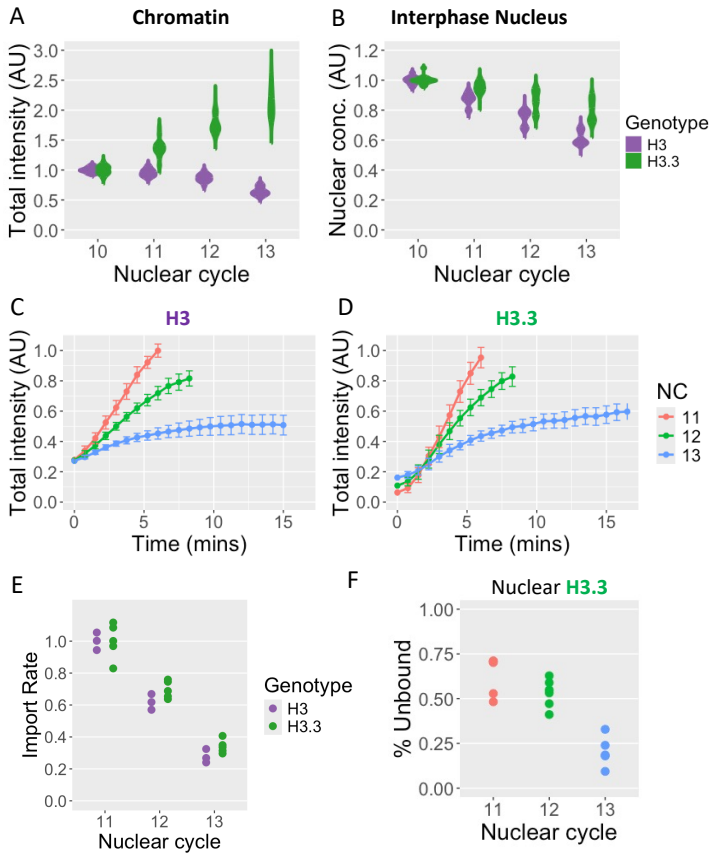

Figure 1: The interphase nuclear availability of H3 decreases more rapidly than H3.3 over the pre-ZGA cycles

(A) Total pixel intensities (amounts) on mitotic chromatin for H3-Dendra2 (purple) and H3.3-Dendra2 (green) between NC10-13 normalized to the average individual NC10 values. Chromatin-bound H3 decreases over NC10-13 whereas H3.3 increases. **(B)** Average interphase nuclear pixel intensities (concentrations) for H3-Dendra2 and H3.3-Dendra2 45 seconds before nuclear envelope breakdown (NEB) in NC10-13, normalized to the average individual NC10 values. H3 and H3.3 concentrations decrease over time, but H3 loss is relatively more rapid. **(C-D)** Total pixel intensities over time for NC11-13 normalized to the maximum NC11 values for H3-Dendra2 **(C)** and H3.3-Dendra2 **(D)**. Nuclear import plateaus after the first 5 mins for H3, but merely slows and does not plateau for H3.3 in NC13. **(E)** Initial slopes of the nuclear import curves shown in C and D for NC11-13. All slopes are normalized to NC11 values. **(F)** The fraction of photoconverted unbound H3.3-Dendra2 after NEB in NC11-13 (see materials and methods for details). The “free” pool of H3.3 falls with each cycle. (n=3 H3 and 5 H3.3 embryos in A-E and >= 5 embryos in F; Statistical comparisons for A, B, and E can be found in Supplemental tables 3-5)

Figure 2: Local N/C ratios differentially affect H3 and H3.3 nuclear import and chromatin incorporation

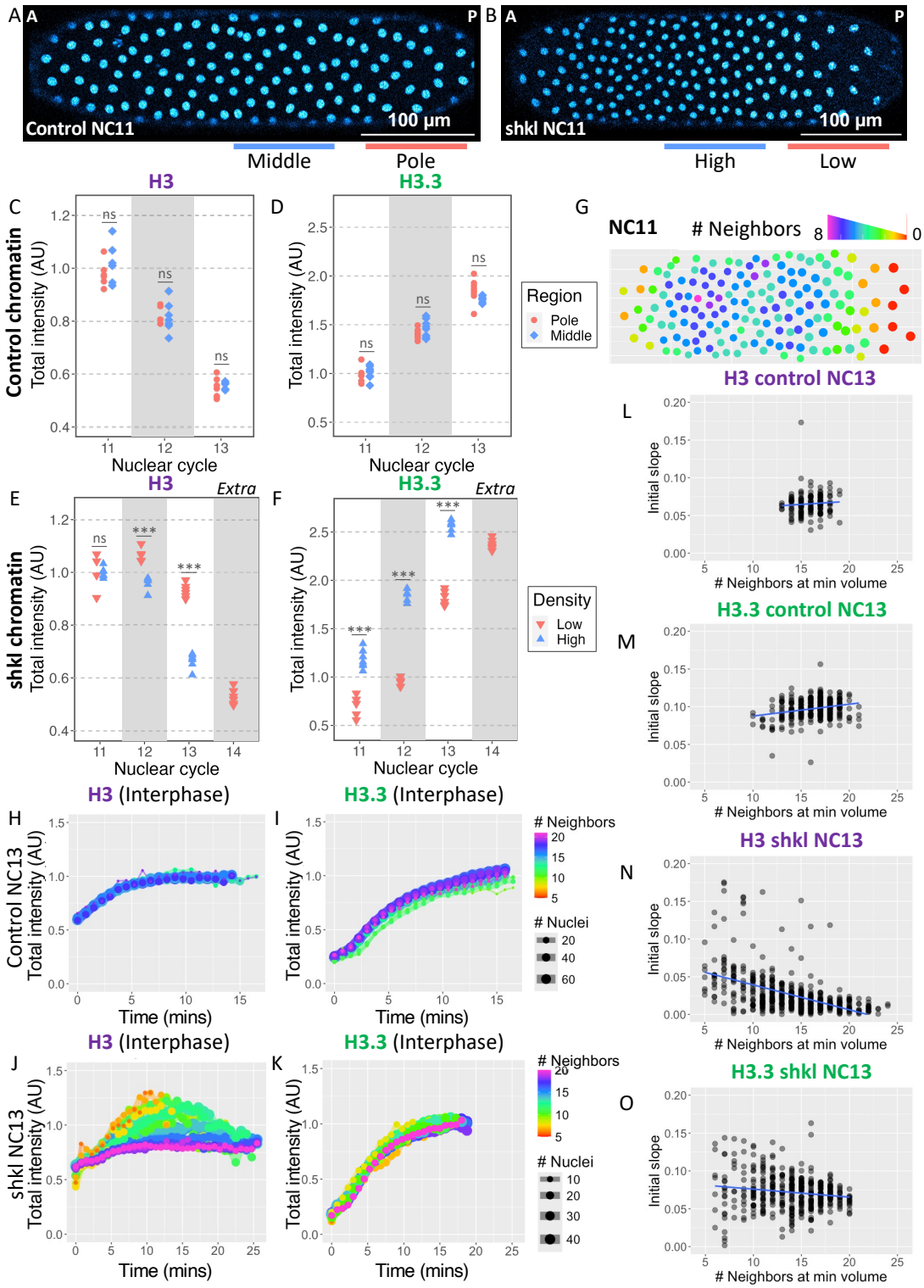

Figure 2: Local N/C ratios differentially affect H3 and H3.3 nuclear import and chromatin incorporation.

(A) Representative NC11 control embryo with middle (blue) and pole (red) regions labeled as used in C and D. **(B)** Representative NC11 shkl embryo with high (blue) and low (red) density regions labeled as used in E and F. **(C-D)** Total intensities on mitotic chromatin of H3-Dendra2 **(C)** and H3.3-Dendra2 **(D)** during NC11-13 in a representative control embryo where each point indicates a single nucleus. Total H3-Dendra2 intensities fall and H3.3-Dendra2 intensities rise uniformly between middle and pole regions within each cycle. **(E-F)** Total intensities on mitotic chromatin of H3-Dendra2 **(E)** and H3.3-Dendra2 **(F)** during NC11-13 in a representative shkl embryo where each point indicates a single nucleus. NC14 represents a partial extra division in the low-density region. Chromatin in the low-density region retains more H3 and incorporates less H3.3 within the same cell cycle compared to the high-density region. Similar results were observed in replicate embryos (Figure S2A-B). **(G)** Gradient in the number of neighbors for each nucleus at its minimum volume within a 20μm radius for the shkl embryo shown in B. **(H-I)** Total intensities over time for nuclei in representative NC13 control embryos binned by the number of neighbors as in G for H3-Dendra2 **(H)** and H3.3-Dendra2 **(I)**. Total intensity was normalized to the average maximum intensities achieved in NC13 and line color represents the number of neighbors. In controls there is little variation in the number of neighbors or the import of H3 and H3.3 across the length of the embryo. **(J-K)** Total intensities over time for nuclei in representative NC13 shkl embryos binned by the number of neighbors as in G for H3-Dendra2 **(J)** and H3.3-Dendra2 **(K)**. Nuclear import and accumulation of H3 inversely correlate with the number of neighbors, suggesting H3 nuclear import is N/C ratio sensitive. H3.3 nuclear import is less N/C ratio sensitive than H3. Similar results were observed in replicate embryos (Figure S2D-G). **(L-M)** Initial slopes of nuclear import curves from representative NC13 control embryos from H and I for H3-Dendra2 **(L)** and H3.3-Dendra2 **(M)** plotted by the number of nuclear neighbors. Note the uniformity in the number of neighbors and similarity in nuclear import behaviors. **(N-O)** Initial slopes of nuclear import curves from representative NC13 shkl embryos from J and K for H3-Dendra2 **(N)** and H3.3-Dendra2 **(O)** plotted by the number of nuclear neighbors. The slopes reflect a faster H3 uptake in nuclei with fewer neighbors and a slower H3 uptake in nuclei with more neighbors. Slopes in some nuclei with more neighbors are near zero indicating that very little additional H3 is imported after nuclear envelope formation. Though the slopes reduce with the number of neighbors for H3.3, there is a non-negligible H3.3 import in the nuclei with the largest number of neighbors. (Statistical significance was determined by 2-way ANOVA, ns= $p>.05$, *** = $p<0.001$)

Figure 3: The chaperone binding site determines H3 variant chromatin incorporation.

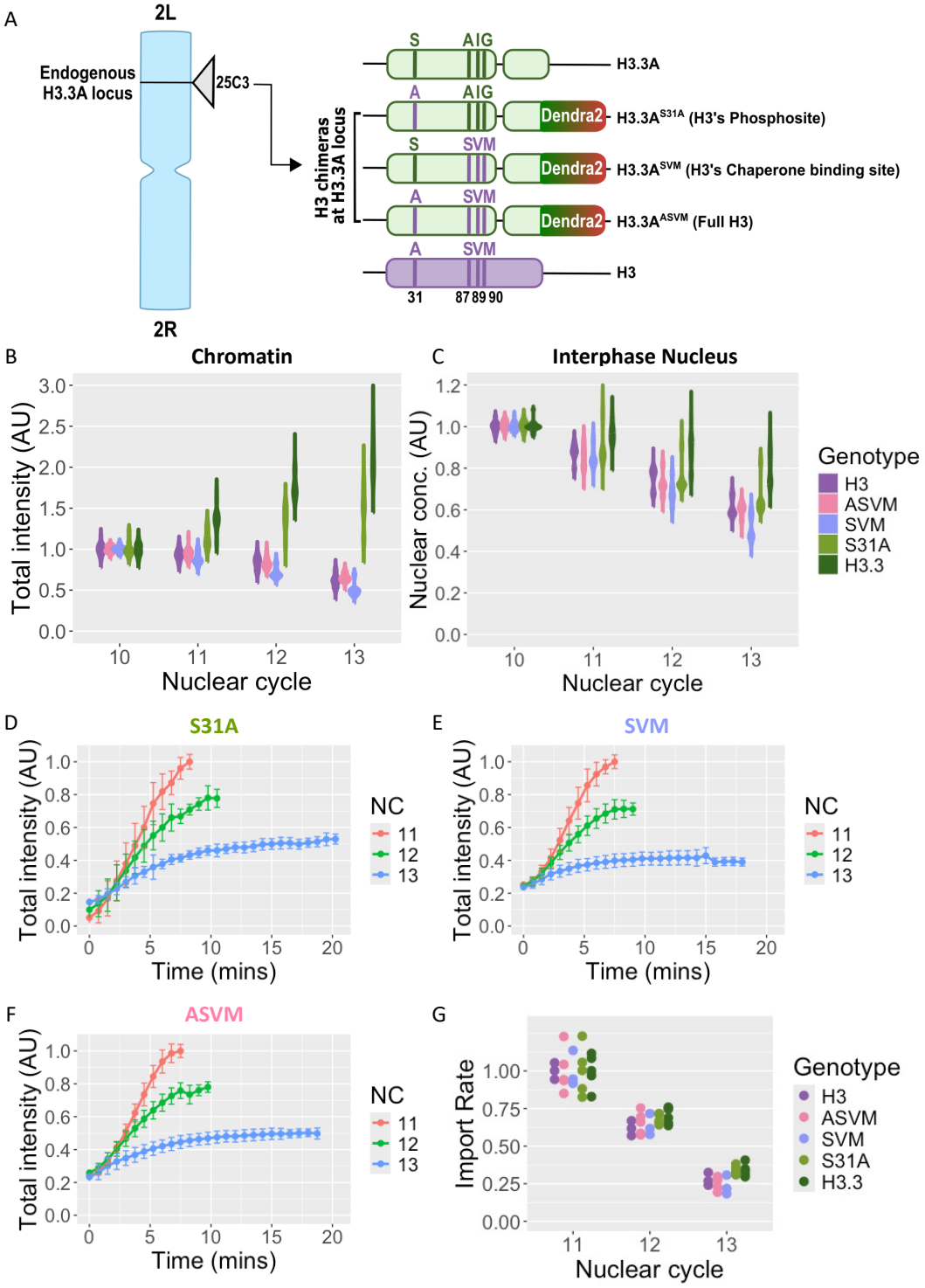

Figure 3: The chaperone binding site determines H3 variant chromatin incorporation. **(A)** Schematic of the Dendra2 tagged H3/H3.3 replacement chimeras at the endogenous H3.3A locus. S31A: H3.3 phosphosite (S) replaced with that of H3 (A), SVM: H3.3 chaperone binding site (AIG) replaced with that of H3 (SVM), and ASVM: all H3.3-specific amino acids replaced with those from H3. **(B)** Total intensities on mitotic chromatin of chimeras during NC10-13 normalized to their NC10 values. H3-Dendra2 and H3.3-Dendra2 from Figure 1A included for reference. $H3.3^{S31A}$ increases similarly to H3.3 while the constructs containing the H3 chaperone binding site decrease similarly to H3. **(C)** Interphase nuclear concentrations of chimeras 45 seconds before NEB during NC10-13 normalized to their NC10 values. H3-Dendra2 and H3.3-Dendra2 from Figure 1B included for reference. As seen for chromatin, nuclear accumulation generally follows the behavior of the chaperone binding site. **(D-F)** Total pixel intensities over time for NC11-13 normalized to the maximum NC11 values for $H3.3^{S31A}$-Dendra2 **(D)**, $H3.3^{SVM}$-Dendra2 **(E)**, and $H3.3^{ASVM}$-Dendra2 **(F).** $H3.3^{S31A}$-Dendra2 import is similar to H3.3-Dendra2, and only slows after 5 minutes without plateauing. $H3.3^{SVM}$-Dendra2 and $H3.3^{ASVM}$-Dendra2 import in a similar manner to H3-Dendra2 and plateau after 5 minutes. **(G)** The initial slopes of nuclear import curves of chimeras shown in D-F for NC11-13. H3-Dendra2 and H3.3-Dendra2 slopes from 1E are included for reference. All slopes are normalized to NC11 values. (n=5 for all chimeras, Statistical comparisons for B, C and G can be found in Supplemental tables 6-8)

Figure 4: Chaperone binding site determines requirement for H3.3 chaperone, Hira

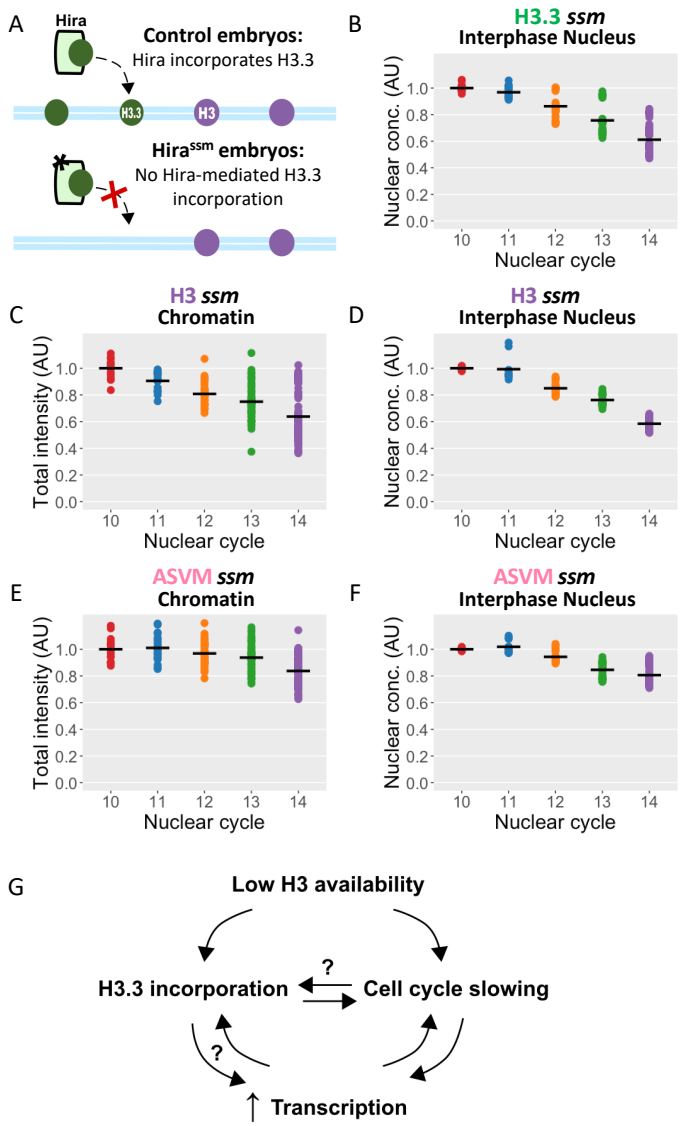

Figure 4: Chaperone binding site determines the requirement for H3.3 chaperone, Hira
(A) Schematic of H3.3 incorporation in control embryos and Hira^{ssm} mutants. H3.3 is imported to the nucleus, but Hira chaperone fails to incorporate H3.3. Hira mutants develop as haploids and undergo one additional fast nuclear division. **(B, D, F)** Average interphase nuclear intensities of H3.3-Dendra2 **(B)**, H3-Dendra2 **(D),** and H3.3^{ASVM}-Dendra2 **(F)** in Hira^{ssm} embryos 45 seconds before the NEB in NC10-14, normalized to their average intensities in NC10. Though H3.3 is not incorporated, it is imported into the nucleus and its concentrations reduce with each cycle. H3 nuclear concentrations also drop with each cycle. However, H3.3^{ASVM} concentrations are relatively more stable over the cycles. **(C, E)** Total intensities of H3-Dendra2 **(C)** and H3.3^{ASVM}-Dendra2 **(E)** on mitotic chromatin in Hira^{ssm} embryos between NC10-14 normalized to their average NC10 values. Though H3.3^{ASVM} is successfully incorporated without active Hira, the chromatin amounts decrease more slowly than H3. **(G)** Direct and indirect mechanisms of H3.3 incorporation upon H3 depletion. H3.3 incorporation could be a direct result of the reduced

nuclear H3 availability. Here, H3 loss would result in missing nucleosomes that are replaced by H3.3. Conversely, the increasing H3.3 incorporation may be a direct or indirect result of the N/C ratio dependent cell cycle slowing. Cell cycle elongation may provide the time necessary for H3.3 to replace H3 directly or through increased transcription or heterochromatin formation. (n=3 H3 ssm, 4 H3.3 ssm, and 5 H3.3^{ASVM} ssm embryos)

Graphical abstract

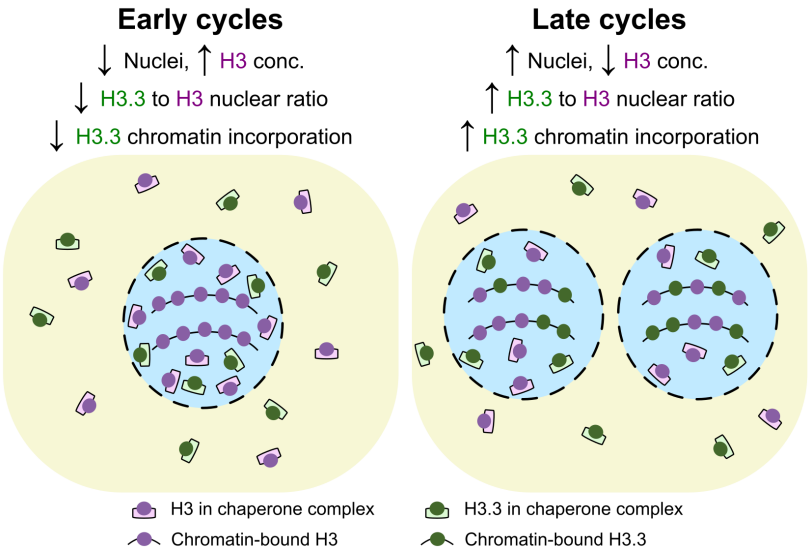

Supplementary Figure 1:Tools and controls underlying image quantification of mitotic and interphase Dendra2 and H3.3 export

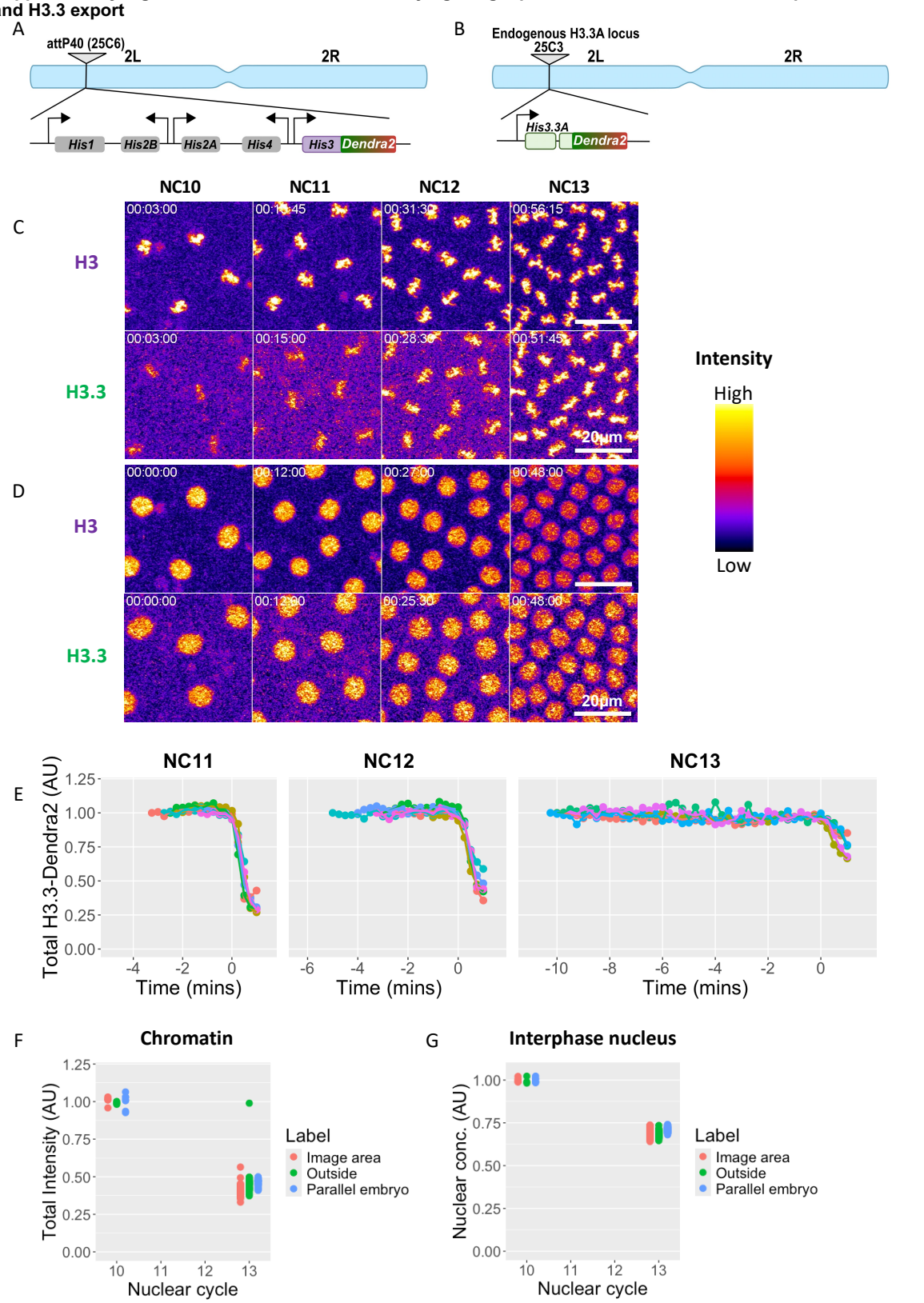

Supplementary Figure 1: Tools and controls underlying image quantification of mitotic and interphase Dendra2 and H3.3 export

(A) A 5kb region containing a single histone gene cluster with one copy of each of the replication-coupled histones including, their promoters, and UTRs as in the endogenous locus in which H3 was N-terminally tagged with the green-to-red photo-switchable fluorophore Dendra2 was inserted at the attp40 site on chromosome 2L (from Shindo and Amodeo, 2019). **(B)** The endogenous H3.3A gene locus was edited to express an N-terminally tagged H3.3-Dendra2 using CRISPR/Cas9 (from Shindo and Amodeo, 2019). **(C)** Maximum intensity projections of H3-Dendra2 (top) and H3.3-Dendra2 (bottom) on mitotic chromatin from NC10-13. Images are pseudo-colored with non-linear look-up tables such that purple indicates low intensities and yellow indicates high intensities. H3 intensities fall and H3.3 intensities rise over the cycles. Chromatin from these embryos are quantified in Figure 1A. **(D)** Maximum intensity projections of H3-Dendra2 (top) and H3.3-Dendra2 (bottom) interphase nucleus 45 seconds before NE breakdown from NC10-13. Images are pseudo-colored as in C. Both H3 and H3.3 intensities drop in the interphase nucleus, but H3.3 intensities drop more slowly than H3. Nuclei from these embryos are quantified in Figure 1B. **(E)** The total pixel intensity of individual photoconverted H3.3-Dendra2 nuclei in NC11-13 (n = 5). Time is shown relative to NEB. H3.3-Dendra2 intensity remains constant before NEB indicating that the nuclear export is negligible. The loss of red signal at NEB represents the pool of unbound H3.3 in the nucleus. Each trace represents a single nucleus, each from different embryos. These data were used to plot the unbound H3.3 in Figure 1F. **(F-G)** Total pixel intensity of H3-Dendra2 on chromatin (F) and interphase nuclei (G) with and without continued laser exposure. Two parallel embryos were used to obtain NC10 and NC13 mitotic chromatin with different levels of laser exposure for photobleaching correction (see methods for details). The 3 regions: 'Image area' corresponds to nuclei imaged throughout NC10-13; 'outside' corresponds to nuclei outside the image area, but within the imaged embryo; and 'parallel embryo' corresponds to nuclei that were only imaged once in NC10 and once in NC13 without continued exposure. Photobleaching was observed to be negligible in experiments quantifying both the mitotic chromatin and interphase nuclear concentration. (Statistical comparisons for F and G can be found in Supplemental tables 1 and 2)

Supplementary Figure 2: Replicate shkl embryos demonstrate consistent effects.

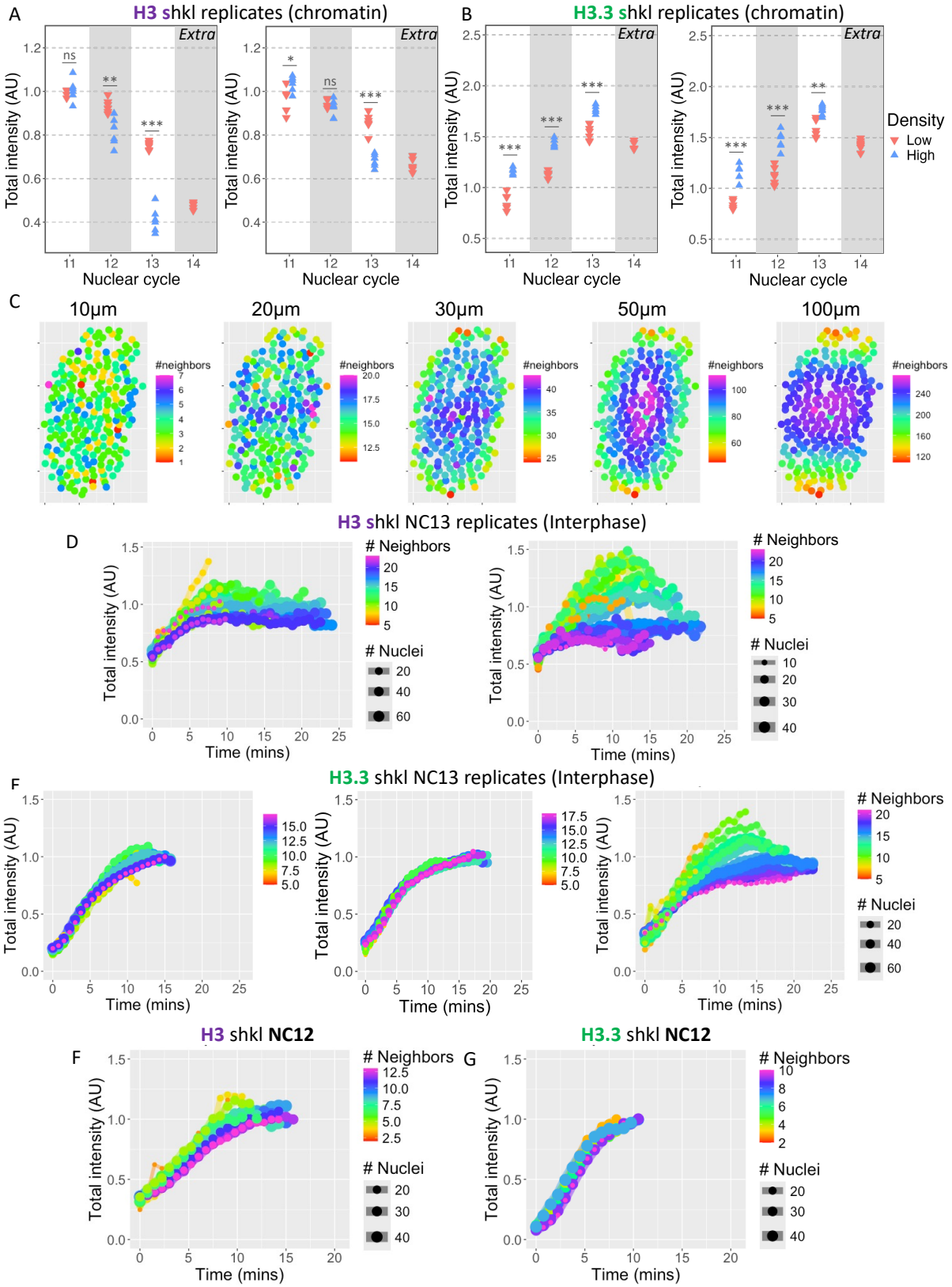

Supplementary Figure 2: Replicate shkl embryos demonstrate consistent effects.
(A) Replicate shkl embryos of the same genotype as shown in Figure 2E demonstrate that H3-Dendra2 is consistently retained on mitotic chromatin by nuclei at low-density regions compared to high-density regions within the same cell cycle over NC11-14. **(B)** Replicate shkl embryos of the same genotype as shown in Figure 2F demonstrate that H3.3-Dendra2 incorporation is reduced on mitotic chromatin by nuclei at low-density regions compared to high-density regions within the same cell cycle over NC11-14. **(C)** Example control embryo in which the radius used to determine the number of neighbors was varied from 10 to 100 μm as shown. A 20 μm radius was deemed optimal for neighborhood analysis as it enabled us to accurately capture the gradient observed in the shkl embryos while excluding edge effects due to embryo curvature. **(D)** Replicate shkl embryos of the same genotype as shown in Figure 2J demonstrate that nuclear import and accumulation of H3 inversely correlate with the number of neighbors surrounding a given nucleus, suggesting H3 nuclear import is N/C ratio sensitive. **(E)** Replicate shkl embryos of the same genotype as shown in Figure 2K demonstrate that nuclear import and accumulation of H3.3 is less N/C ratio sensitive than H3 in most cases. **(F-G)** Total intensities over time for H3-Dendra2 (F) and H3.3-Dendra2 (G) in NC12 shkl embryos indicate that the trends observed in NC13 begin in NC12 though to a lesser extent. These data were taken from the same embryo that was used in Figure 2J and K respectively. (Statistical significance was determined by 2-way ANOVA, ns= $p>.05$, *=$p<.05$, **=$p<0.01$, *** = $p<0.001$)

Supplementary Figure 3: Representative images of H3/H3.3 chimeras

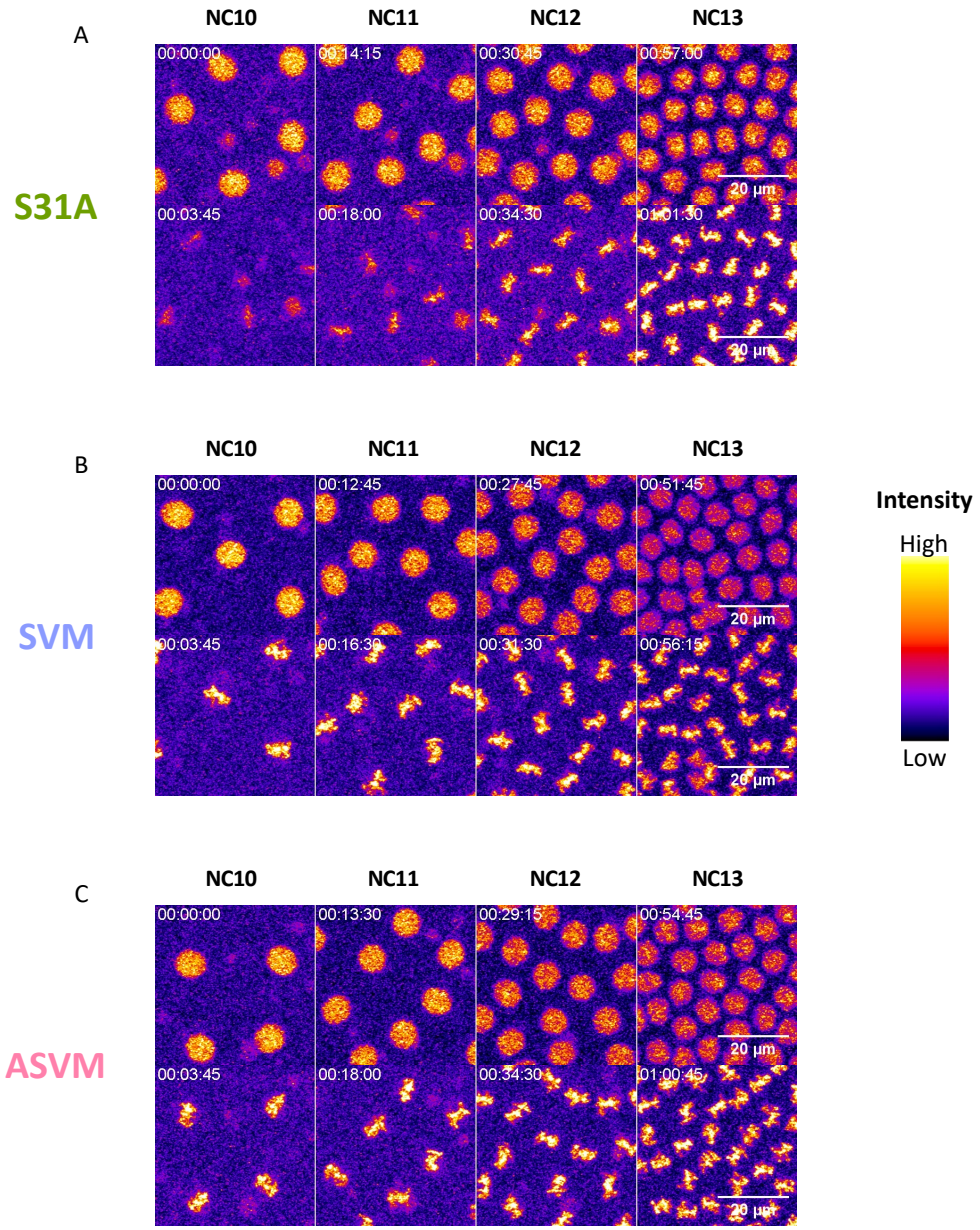

Supplementary Figure 3: Representative images of H3/H3.3 chimeras
(A) Representative maximum intensity projections of H3.3^{S31A}-Dendra2 during interphase and mitosis over NC10-13: interphase nuclei (top) and mitotic chromatin (bottom). Images are pseudo-colored with non-linear look-up tables such that purple indicates low intensities and yellow indicates high intensities. H3.3^{S31A} behaves similarly to H3.3. Data from these embryos are quantified in Figure 3. **(B)** Representative maximum intensity projections of H3.3^{SVM}-Dendra2 during interphase and mitosis over NC10-13: interphase nuclei (top) and mitotic chromatin (bottom). H3.3^{SVM} behaves similarly to H3. Data from these embryos are quantified in Figure 3. **(C)** Representative maximum intensity projections of H3.3^{ASVM}-Dendra2 during interphase and mitosis over NC10-13: interphase nuclei (top) and mitotic chromatin (bottom). H3.3^{ASVM} behaves similarly to H3. Data from these embryos are quantified in Figure 3.

Supplementary Figure 4: Representative images of H3, H3.3, and H3.3^{ASVM} in Hira mutants

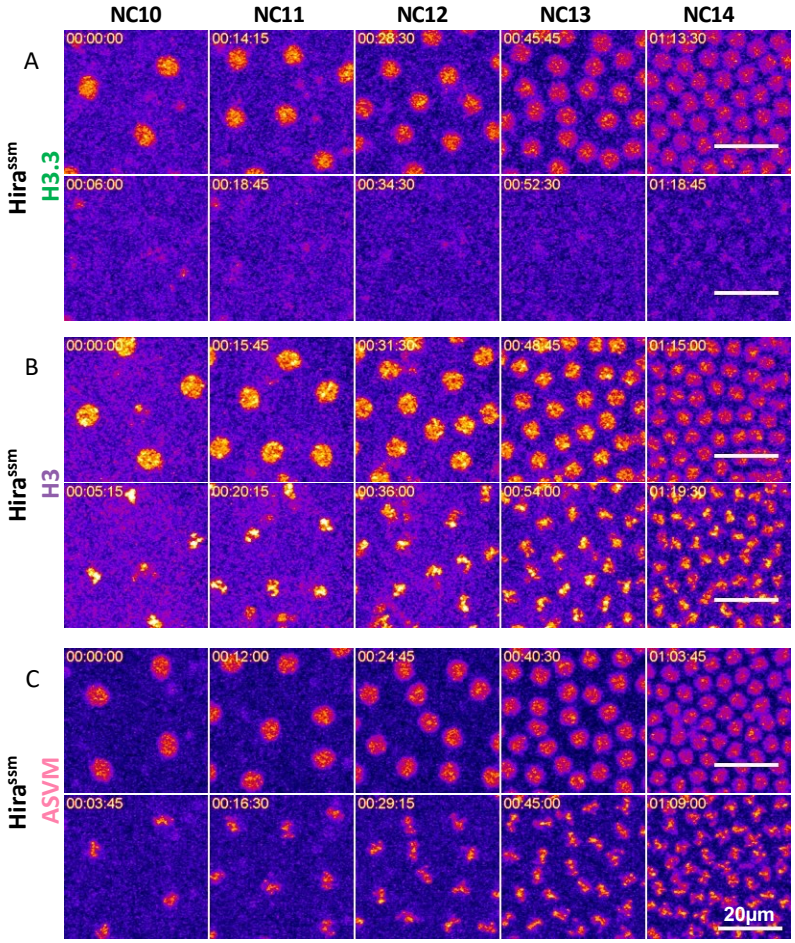

Supplementary Figure 4: Representative images of H3, H3.3, and H3.3^{ASVM} in Hira mutants
(A) Representative maximum intensity projections of H3.3-Dendra2 during interphase and mitosis over NC10-13: interphase nuclei (top) and mitotic chromatin (bottom). Images are pseudo-colored with non-linear look-up tables such that purple indicates low intensities and yellow indicates high intensities. H3.3 is unable to be incorporated into chromatin but is still imported into the nucleus. Data from these embryos are quantified in Figure 4B.
(B) Representative maximum intensity projections of H3-Dendra2 during interphase and mitosis over NC10-13: interphase nuclei (top) and mitotic chromatin (bottom). H3 continues to accumulate on chromatin in the absence of Hira. Data from these embryos are quantified in Figure 4C and D. **(C)** Representative maximum intensity projections of H3.3^{ASVM}-Dendra2 during interphase and mitosis over NC10-13: interphase nuclei (top) and mitotic chromatin (bottom). H3.3^{ASVM} continues to accumulate on chromatin in the absence of Hira. Data from these embryos are quantified in Figure 4E and F.

Supplementary tables

Supplementary Table S1: 2-way ANOVA results for the different regions in the parallel embryo experiment for photobleaching correction for chromatin (NC10 vs NC13) as shown in Figure S1G.

Comparison groups	Difference in means	Adjusted p-value
NC10_Outside - NC10_Image area	-0.015039	0.99820702
NC10_Parallel embryo - NC10_Image area	-0.006684	0.99993379
NC10_Parallel embryo - NC10_Outside	0.00835498	0.99985763
NC13_Outside - NC13_Image area	0.05703447	2.35E-06
NC13_Parallel embryo - NC13_Image area	0.05682858	2.58E-06
NC13_Parallel embryo - NC13_Outside	-0.0002059	1
NC13_Image area - NC10_Image area	-0.6050886	0
NC13_Outside - NC10_Outside	-0.5330152	0
NC13_Parallel embryo - NC10_Parallel embryo	-0.5415761	0

Supplementary Table S2: 2-way ANOVA results for the different regions in the parallel embryo experiment for photobleaching correction for interphase nuclear concentration (NC10 vs NC13) as shown in Figure S1F.

Comparison groups	Difference in means	Adjusted p-value
NC10_Outside - NC10_Image area	-0.0030836	0.99990859
NC10_Parallel embryo - NC10_Image area	-0.0011564	0.99999823
NC10_Parallel embryo - NC10_Outside	0.00192728	0.99998957
NC13_Outside - NC13_Image area	-0.004531	0.6781679
NC13_Parallel embryo - NC13_Image area	0.02075448	1.31E-11
NC13_Parallel embryo - NC13_Outside	0.02528553	1.73E-12
NC13_Image area - NC10_Image area	-0.3123329	9.00E-14
NC13_Outside - NC10_Outside	-0.3137803	9.00E-14
NC13_Parallel embryo - NC10_Parallel embryo	-0.2904221	9.00E-14

Supplementary Table S3: 2-way ANOVA results of H3-Dendra2 and H3.3-Dendra2 on chromatin over NC10 - NC13 as shown in Figure 1A.

Comparison groups	Difference in means	Adjusted p-value
NC11_H3 - NC10_H3	-0.0635616	0.84535671
NC12_H3 - NC11_H3	-0.0960586	0.13632753
NC13_H3 - NC12_H3	-0.2217689	0
NC11_H3.3 - NC10_H3.3	0.36765264	0
NC12_H3.3 - NC11_H3.3	0.40334239	0
NC13_H3.3 - NC12_H3.3	0.3693797	0

Supplementary Table S4: 2-way ANOVA results of H3-Dendra2 and H3.3-Dendra2 nuclear concentrations in the interphase nucleus during NC10 - NC13 as shown in Figure 1B.

Comparison groups	Difference in means	Adjusted p-value
NC11_H3 - NC10_H3	-0.1279587	0
NC12_H3 - NC11_H3	-0.1262473	0
NC13_H3 - NC12_H3	-0.1349846	0
NC11_H3.3 - NC10_H3.3	-0.0196737	0.9180396
NC12_H3.3 - NC11_H3.3	-0.076703	0
NC13_H3.3 - NC12_H3.3	-0.0847695	0

Supplementary Table S5: 2-way ANOVA results of initial H3-Dendra2 and H3.3-Dendra2 import rates during NC11 - NC13 as shown in Figure 1E.

Comparison groups	Difference in means	Adjusted p-value
NC12_H3 - NC11_H3	-0.381055416	0.00016788
NC12_H3.3 - NC11_H3.3	-0.303255393	0.00010136
NC13_H3 - NC12_H3	-0.34119875	0.00110214
NC13_H3.3 - NC12_H3.3	-0.356357728	3.46E-06
NC12_H3.3 - NC12_H3	0.077800023	0.99461495
NC13_H3.3 - NC13_H3	0.062641045	0.99943292

Supplementary Table S6: 2-way ANOVA results of chimeras compared to H3-Dendra2 and H3.3-Dendra2 on chromatin over NC10 - NC13 as shown in Figure 3B.

Comparison groups	Difference in means	Adjusted p-value
NC10_H3 - NC10_ASVM	3.89E-15	1
NC10_H3.3 - NC10_ASVM	1.67E-15	1
NC10_S31A - NC10_ASVM	1.67E-15	1
NC10_SVM - NC10_ASVM	-9.99E-16	1
NC10_H3.3 - NC10_H3	-2.22E-15	1
NC10_S31A - NC10_H3	-2.22E-15	1
NC10_SVM - NC10_H3	-4.88E-15	1
NC10_S31A - NC10_H3.3	0	1
NC10_SVM - NC10_H3.3	-2.66E-15	1
NC10_SVM - NC10_S31A	-2.66E-15	1
NC11_H3 - NC11_ASVM	-0.0068851	1
NC11_H3.3 - NC11_ASVM	0.4243291	4.25E-13
NC11_S31A - NC11_ASVM	0.1840243	0.00025578
NC11_SVM - NC11_ASVM	-0.0517242	0.99824718
NC11_H3.3 - NC11_H3	0.43121424	4.25E-13
NC11_S31A - NC11_H3	0.19090943	0.00016407

NC11_SVM - NC11_H3	-0.0448391	0.99981202
NC11_S31A - NC11_H3.3	-0.2403048	2.73E-08
NC11_SVM - NC11_H3.3	-0.4760533	4.25E-13
NC11_SVM - NC11_S31A	-0.2357485	4.12E-07
NC12_H3 - NC12_ASVM	0.01024074	1
NC12_H3.3 - NC12_ASVM	0.940856	4.25E-13
NC12_S31A - NC12_ASVM	0.53949536	4.25E-13
NC12_SVM - NC12_ASVM	-0.1116121	0.00861526
NC12_H3.3 - NC12_H3	0.93061526	4.25E-13
NC12_S31A - NC12_H3	0.52925461	4.25E-13
NC12_SVM - NC12_H3	-0.1218529	0.00136736
NC12_S31A - NC12_H3.3	-0.4013606	4.25E-13
NC12_SVM - NC12_H3.3	-1.0524681	4.25E-13
NC12_SVM - NC12_S31A	-0.6511075	4.25E-13
NC13_H3 - NC13_ASVM	-0.0396914	0.87634119
NC13_H3.3 - NC13_ASVM	1.48207247	4.25E-13
NC13_S31A - NC13_ASVM	0.84790992	4.25E-13
NC13_SVM - NC13_ASVM	-0.1483188	2.14E-11
NC13_H3.3 - NC13_H3	1.5217639	4.25E-13
NC13_S31A - NC13_H3	0.88760135	4.25E-13
NC13_SVM - NC13_H3	-0.1086274	3.31E-06
NC13_S31A - NC13_H3.3	-0.6341626	4.25E-13
NC13_SVM - NC13_H3.3	-1.6303913	4.25E-13
NC13_SVM - NC13_S31A	-0.9962288	4.25E-13

Supplementary Table S7: 2-way ANOVA results for nuclear concentrations of chimeras compared to H3-Dendra2 and H3.3-Dendra2 in the interphase nucleus during NC10 - NC13 as shown in Figure 3C.

Comparison groups	Difference in Means	Adjusted p-value
NC10_H3 - NC10_ASVM	-0.0065242	1
NC10_H3.3 - NC10_ASVM	-0.0065242	1
NC10_S31A - NC10_ASVM	0.00742142	1
NC10_SVM - NC10_ASVM	-0.0065242	1
NC10_H3.3 - NC10_H3	4.79E-11	1
NC10_S31A - NC10_H3	0.01394559	0.99999911
NC10_SVM - NC10_H3	-6.10E-12	1
NC10_S31A - NC10_H3.3	0.01394559	0.99999995
NC10_SVM - NC10_H3.3	-5.40E-11	1
NC11_H3 - NC11_ASVM	0.01667171	0.97989387
NC11_H3.3 - NC11_ASVM	0.12495672	2.09E-09

NC11_S31A - NC11_ASVM	0.05364774	2.32E-07
NC11_SVM - NC11_ASVM	-0.002033	1
NC11_H3.3 - NC11_H3	0.10828501	2.09E-09
NC11_S31A - NC11_H3	0.03697603	0.04475264
NC11_SVM - NC11_H3	-0.0187047	0.93967111
NC11_S31A - NC11_H3.3	-0.071309	2.09E-09
NC11_SVM - NC11_H3.3	-0.1269897	2.09E-09
NC11_SVM - NC11_S31A	-0.0556807	6.92E-08
NC12_H3 - NC12_ASVM	0.02127928	0.20956792
NC12_H3.3 - NC12_ASVM	0.17910857	2.09E-09
NC12_S31A - NC12_ASVM	0.03514949	2.23E-06
NC12_SVM - NC12_ASVM	-0.040491	2.52E-08
NC12_H3.3 - NC12_H3	0.15782929	2.09E-09
NC12_S31A - NC12_H3	0.0138702	0.92077642
NC12_SVM - NC12_H3	-0.0617703	2.09E-09
NC12_S31A - NC12_H3.3	-0.1439591	2.09E-09
NC12_SVM - NC12_H3.3	-0.2195996	2.09E-09
NC12_SVM - NC12_S31A	-0.0756405	2.09E-09
NC13_H3 - NC13_ASVM	0.00938645	0.94556903
NC13_H3.3 - NC13_ASVM	0.21743081	2.09E-09
NC13_S31A - NC13_ASVM	0.05957505	2.09E-09
NC13_SVM - NC13_ASVM	-0.0865556	2.09E-09
NC13_H3.3 - NC13_H3	0.20804436	2.09E-09
NC13_S31A - NC13_H3	0.0501886	2.09E-09
NC13_SVM - NC13_H3	-0.095942	2.09E-09
NC13_S31A - NC13_H3.3	-0.1578558	2.09E-09
NC13_SVM - NC13_H3.3	-0.3039864	2.09E-09
NC13_SVM - NC13_S31A	-0.1461306	2.09E-09

Supplementary Table S8: 2-way ANOVA results of initial import rates of chimeras compared to H3-Dendra2 and H3.3-Dendra2 during NC11 - NC13 as shown in Figure 3G.

Comparison groups	Difference in Means	Adjusted p-value
NC12_ASVM - NC11_ASVM	-0.346793281	6.39E-06
NC12_H3 - NC11_H3	-0.381055416	0.00016788
NC12_H3.3 - NC11_H3.3	-0.303255393	0.00010136
NC12_S31A - NC11_S31A	-0.320997327	3.31E-05
NC12_SVM - NC11_SVM	-0.363066437	0.0003963
NC13_ASVM - NC12_ASVM	-0.398034537	2.36E-07
NC13_H3 - NC12_H3	-0.34119875	0.00110214
NC13_H3.3 - NC12_H3.3	-0.356357728	3.46E-06

NC13_S31A - NC12_S31A	-0.341763381	8.82E-06
NC13_SVM - NC12_SVM	-0.400466562	6.55E-05
NC13_SVM - NC13_ASVM	-0.018705181	1
NC13_SVM - NC13_H3	-0.041278832	0.99999904
NC12_ASVM - NC12_H3	0.034262135	0.99999964
NC12_H3.3 - NC12_ASVM	0.043537888	0.99995511
NC12_H3.3 - NC12_H3	0.077800023	0.99461495
NC12_H3.3 - NC12_S31A	0.017741934	1
NC12_H3.3 - NC12_SVM	0.059811044	0.99966109
NC12_S31A - NC12_ASVM	0.025795954	0.99999994
NC12_S31A - NC12_H3	0.060058089	0.99964501
NC12_S31A - NC12_SVM	0.04206911	0.99999497
NC12_SVM - NC12_ASVM	-0.016273156	1
NC12_SVM - NC12_H3	0.017988979	1
NC13_ASVM - NC13_H3	-0.022573651	1
NC13_H3.3 - NC13_ASVM	0.085214697	0.95767702
NC13_H3.3 - NC13_H3	0.062641045	0.99943292
NC13_H3.3 - NC13_S31A	0.003147587	1
NC13_H3.3 - NC13_SVM	0.103919878	0.93613851
NC13_S31A - NC13_ASVM	0.082067109	0.96862842
NC13_S31A - NC13_H3	0.059493458	0.99968081
NC13_S31A - NC13_SVM	0.100772291	0.94917367

References

1. Khorasanizadeh, S. (2004). The Nucleosome: From Genomic Organization to Genomic Regulation. Cell *116*, 259–272. https://doi.org/10.1016/S0092-8674(04)00044-3.

2. Talbert, P.B., and Henikoff, S. (2017). Histone variants on the move: substrates for chromatin dynamics. Nat Rev Mol Cell Biol *18*, 115–126. https://doi.org/10.1038/nrm.2016.148.

3. Talbert, P.B., and Henikoff, S. (2021). Histone variants at a glance. Journal of Cell Science *134*. https://doi.org/10.1242/jcs.244749.

4. Weber, C.M., and Henikoff, S. (2014). Histone variants: dynamic punctuation in transcription. Genes Dev. *28*, 672–682. https://doi.org/10.1101/gad.238873.114.

5. Loppin, B., and Berger, F. (2020). Histone Variants: The Nexus of Developmental Decisions and Epigenetic Memory. Annual Review of Genetics *54*, 121–149. https://doi.org/10.1146/annurev-genet-022620-100039.

6. Lifton, R.P., Goldberg, M.L., Karp, R.W., and Hogness, D.S. (1978). The Organization of the Histone Genes in Drosophila melanogaster: Functional and Evolutionary Implications. Cold Spring Harb Symp Quant Biol *42*, 1047–1051. https://doi.org/10.1101/SQB.1978.042.01.105.

7. Marzluff, W.F., Wagner, E.J., and Duronio, R.J. (2008). Metabolism and regulation of canonical histone mRNAs: life without a poly(A) tail. Nat Rev Genet *9*, 843–854. https://doi.org/10.1038/nrg2438.

8. McKay, D.J., Klusza, S., Penke, T.J.R., Meers, M.P., Curry, K.P., McDaniel, S.L., Malek, P.Y., Cooper, S.W., Tatomer, D.C., Lieb, J.D., et al. (2015). Interrogating the Function of Metazoan Histones using Engineered Gene Clusters. Developmental Cell *32*, 373–386. https://doi.org/10.1016/j.devcel.2014.12.025.

9. Dominski, Z., and Tong, L. (2021). U7 deciphered: the mechanism that forms the unusual 3’ end of metazoan replication-dependent histone mRNAs. Biochem Soc Trans *49*, 2229–2240. https://doi.org/10.1042/BST20210323.

10. Talbert, P.B., and Henikoff, S. (2010). Histone variants — ancient wrap artists of the epigenome. Nat Rev Mol Cell Biol *11*, 264–275. https://doi.org/10.1038/nrm2861.

11. Shindo, Y., Brown, M.G., and Amodeo, A.A. (2022). Versatile roles for histones in early development. Current Opinion in Cell Biology *75*, 102069. https://doi.org/10.1016/j.ceb.2022.02.003.

12. Dimitrov, S., Almouzni, G., Dasso, M., and Wolffe, A.P. (1993). Chromatin Transitions during Early *Xenopus* Embryogenesis: Changes in Histone H4 Acetylation and in Linker Histone Type. Developmental Biology *160*, 214–227. https://doi.org/10.1006/dbio.1993.1299.

13. Pérez-Montero, S., Carbonell, A., Morán, T., Vaquero, A., and Azorín, F. (2013). The Embryonic Linker Histone H1 Variant of *Drosophila*, dBigH1, Regulates Zygotic Genome Activation. Developmental Cell *26*, 578–590. https://doi.org/10.1016/j.devcel.2013.08.011.

14. Müller, K., Thisse, C., Thisse, B., and Raz, E. (2002). Expression of a linker histone-like gene in the primordial germ cells in zebrafish. Mechanisms of Development *117*, 253–257. https://doi.org/10.1016/S0925-4773(02)00174-0.

15. Johnson, M.R., Stephenson, R.A., Ghaemmaghami, S., and Welte, M.A. Developmentally regulated H2Av buffering via dynamic sequestration to lipid droplets in Drosophila embryos. eLife *7*, e36021. https://doi.org/10.7554/eLife.36021.

16. Smith, R.C., Dworkin-Rastl, E., and Dworkin, M.B. (1988). Expression of a histone H1-like protein is restricted to early Xenopus development. Genes Dev *2*, 1284–1295. https://doi.org/10.1101/gad.2.10.1284.

17. Wibrand, K., and Olsen, L.C. (2002). Linker histone *H1M* transcripts mark the developing germ line in zebrafish. Mechanisms of Development *117*, 249–252. https://doi.org/10.1016/S0925-4773(02)00173-9.

18. Tadros, W., and Lipshitz, H.D. (2009). The maternal-to-zygotic transition: a play in two acts. Development *136*, 3033–3042. https://doi.org/10.1242/dev.033183.

19. Vastenhouw, N.L., Cao, W.X., and Lipshitz, H.D. (2019). The maternal-to-zygotic transition revisited. Development *146*, dev161471. https://doi.org/10.1242/dev.161471.

20. Blythe, S.A., and Wieschaus, E.F. (2016). Establishment and maintenance of heritable chromatin structure during early Drosophila embryogenesis. eLife *5*, e20148. https://doi.org/10.7554/eLife.20148.

21. Seller, C.A., Cho, C.-Y., and O'Farrell, P.H. (2019). Rapid embryonic cell cycles defer the establishment of heterochromatin by Eggless/SetDB1 in Drosophila. Genes Dev. https://doi.org/10.1101/gad.321646.118.

22. Hug, C.B., Grimaldi, A.G., Kruse, K., and Vaquerizas, J.M. (2017). Chromatin Architecture Emerges during Zygotic Genome Activation Independent of Transcription. Cell *169*, 216-228.e19. https://doi.org/10.1016/j.cell.2017.03.024.

23. Shermoen, A.W., McCleland, M.L., and O'Farrell, P.H. (2010). Developmental Control of Late Replication and S phase Length. Curr Biol *20*, 2067–2077. https://doi.org/10.1016/j.cub.2010.10.021.

24. McKnight, S.L., and Miller, O.L. (1977). Electron microscopic analysis of chromatin replication in the cellular blastoderm drosophila melanogaster embryo. Cell *12*, 795–804. https://doi.org/10.1016/0092-8674(77)90278-1.

25. Zhang, Y., Vastenhouw, N.L., Feng, J., Fu, K., Wang, C., Ge, Y., Pauli, A., van Hummelen, P., Schier, A.F., and Liu, X.S. (2014). Canonical nucleosome organization at promoters forms during genome activation. Genome Res *24*, 260–266. https://doi.org/10.1101/gr.157750.113.

26. Horard, B., and Loppin, B. (2015). Histone storage and deposition in the early Drosophila embryo. Chromosoma *124*, 163–175. https://doi.org/10.1007/s00412-014-0504-7.

27. Adamson, E.D., and Woodland, H.R. (1974). Histone synthesis in early amphibian development: Histone and DNA syntheses are not co-ordinated. Journal of Molecular Biology *88*, 263–285. https://doi.org/10.1016/0022-2836(74)90481-1.

28. Woodland, H.R., and Adamson, E.D. (1977). The synthesis and storage of histones during the oogenesis of Xenopus laevis. Dev Biol *57*, 118–135. https://doi.org/10.1016/0012-1606(77)90359-1.

29. Shindo, Y., and Amodeo, A.A. (2019). Dynamics of Free and Chromatin-Bound Histone H3 during Early Embryogenesis. Current Biology *29*, 359-366.e4. https://doi.org/10.1016/j.cub.2018.12.020.

30. Farrell, J.A., and O'Farrell, P.H. (2014). From Egg to Gastrula: How the Cell Cycle Is Remodeled During the Drosophila Mid-Blastula Transition. Annual Review of Genetics *48*, 269–294. https://doi.org/10.1146/annurev-genet-111212-133531.

31. Farrell, J.A., and O'Farrell, P.H. (2014). From egg to gastrula: how the cell cycle is remodeled during the Drosophila mid-blastula transition. Annu Rev Genet *48*, 269–294. https://doi.org/10.1146/annurev-genet-111212-133531.

32. Newport, J., and Kirschner, M. (1982). A major developmental transition in early Xenopus embryos: I. characterization and timing of cellular changes at the midblastula stage. Cell *30*, 675–686. https://doi.org/10.1016/0092-8674(82)90272-0.

33. Newport, J., and Kirschner, M. (1982). A major developmental transition in early Xenopus embryos: II. Control of the onset of transcription. Cell *30*, 687–696. https://doi.org/10.1016/0092-8674(82)90273-2.

34. Kane, D.A., and Kimmel, C.B. (1993). The zebrafish midblastula transition. Development *119*, 447–456. https://doi.org/10.1242/dev.119.2.447.

35. Blythe, S.A., and Wieschaus, E.F. (2015). Chapter Four - Coordinating Cell Cycle Remodeling with Transcriptional Activation at the Drosophila MBT. In Current Topics in Developmental Biology The Maternal-to-Zygotic Transition., H. D. Lipshitz, ed. (Academic Press), pp. 113–148. https://doi.org/10.1016/bs.ctdb.2015.06.002.

36. Amodeo, A.A., Jukam, D., Straight, A.F., and Skotheim, J.M. (2015). Histone titration against the genome sets the DNA-to-cytoplasm threshold for the Xenopus

midblastula transition. Proceedings of the National Academy of Sciences *112*, E1086–E1095. https://doi.org/10.1073/pnas.1413990112.

37. Chari, S., Wilky, H., Govindan, J., and Amodeo, A.A. (2019). Histone concentration regulates the cell cycle and transcription in early development. Development *146*, dev177402. https://doi.org/10.1242/dev.177402.

38. Shindo, Y., and Amodeo, A.A. (2021). Excess histone H3 is a competitive Chk1 inhibitor that controls cell-cycle remodeling in the early Drosophila embryo. Current Biology *31*, 2633-2642.e6. https://doi.org/10.1016/j.cub.2021.03.035.

39. Almouzni, G., Méchali, M., and Wolffe, A.P. (1990). Competition between transcription complex assembly and chromatin assembly on replicating DNA. The EMBO Journal *9*, 573–582. https://doi.org/10.1002/j.1460-2075.1990.tb08145.x.

40. Almouzni, G., Méchali, M., and Wolffe, A.P. (1991). Transcription Complex Disruption Caused by a Transition in Chromatin Structure. Molecular and Cellular Biology *11*, 655–665. https://doi.org/10.1128/mcb.11.2.655-665.1991.

41. Prioleau, M.N., Huet, J., Sentenac, A., and Méchali, M. (1994). Competition between chromatin and transcription complex assembly regulates gene expression during early development. Cell *77*, 439–449. https://doi.org/10.1016/0092-8674(94)90158-9.

42. Almouzni, G., and Wolffe, A.P. (1995). Constraints on transcriptional activator function contribute to transcriptional quiescence during early Xenopus embryogenesis. EMBO J *14*, 1752–1765.

43. Joseph, S.R., Pálfy, M., Hilbert, L., Kumar, M., Karschau, J., Zaburdaev, V., Shevchenko, A., and Vastenhouw, N.L. (2017). Competition between histone and transcription factor binding regulates the onset of transcription in zebrafish embryos. eLife *6*, e23326. https://doi.org/10.7554/eLife.23326.

44. Li, Z., Johnson, M.R., Ke, Z., Chen, L., and Welte, M.A. (2014). *Drosophila* Lipid Droplets Buffer the H2Av Supply to Protect Early Embryonic Development. Current Biology *24*, 1485–1491. https://doi.org/10.1016/j.cub.2014.05.022.

45. Santenard, A., Ziegler-Birling, C., Koch, M., Tora, L., Bannister, A.J., and Torres-Padilla, M.-E. (2010). Heterochromatin formation in the mouse embryo requires critical residues of the histone variant H3.3. Nat Cell Biol *12*, 853–862. https://doi.org/10.1038/ncb2089.

46. Jang, C.-W., Shibata, Y., Starmer, J., Yee, D., and Magnuson, T. (2015). Histone H3.3 maintains genome integrity during mammalian development. Genes Dev *29*, 1377–1392. https://doi.org/10.1101/gad.264150.115.

47. Klein, R.H., and Knoepfler, P.S. (2023). Knockout tales: the versatile roles of histone H3.3 in development and disease. Epigenetics & Chromatin *16*, 38. https://doi.org/10.1186/s13072-023-00512-8.

48. Sitbon, D., Boyarchuk, E., Dingli, F., Loew, D., and Almouzni, G. (2020). Histone variant H3.3 residue S31 is essential for Xenopus gastrulation regardless of the deposition pathway. Nat Commun *11*, 1256. https://doi.org/10.1038/s41467-020-15084-4.

49. Delaney, K., Weiss, N., and Almouzni, G. (2023). The cell-cycle choreography of H3 variants shapes the genome. Molecular Cell *83*, 3773–3786. https://doi.org/10.1016/j.molcel.2023.08.030.

50. Sakai, A., Schwartz, B.E., Goldstein, S., and Ahmad, K. (2009). Transcriptional and developmental functions of the H3. 3 histone variant in Drosophila. Current Biology *19*, 1816–1820.

51. Hödl, M., and Basler, K. (2009). Transcription in the absence of histone H3.3. Curr Biol *19*, 1221–1226. https://doi.org/10.1016/j.cub.2009.05.048.

52. Szenker, E., Ray-Gallet, D., and Almouzni, G. (2011). The double face of the histone variant H3. 3. Cell research *21*, 421–434.

53. Hayden, L., Chao, A., Deneke, V.E., Vergassola, M., Puliafito, A., and Di Talia, S. (2022). Cullin-5 mutants reveal collective sensing of the nucleocytoplasmic ratio in Drosophila embryogenesis. Curr Biol *32*, 2084-2092.e4. https://doi.org/10.1016/j.cub.2022.03.007.

54. Tagami, H., Ray-Gallet, D., Almouzni, G., and Nakatani, Y. (2004). Histone H3. 1 and H3. 3 complexes mediate nucleosome assembly pathways dependent or independent of DNA synthesis. Cell *116*, 51–61.

55. Loppin, B., Docquier, M., Bonneton, F., and Couble, P. (2000). The Maternal Effect Mutation sésame Affects the Formation of the Male Pronucleus in Drosophila melanogaster. Developmental Biology *222*, 392–404. https://doi.org/10.1006/dbio.2000.9718.

56. Ray-Gallet, D., Woolfe, A., Vassias, I., Pellentz, C., Lacoste, N., Puri, A., Schultz, D.C., Pchelintsev, N.A., Adams, P.D., Jansen, L.E.T., et al. (2011). Dynamics of histone H3 deposition in vivo reveal a nucleosome gap-filling mechanism for H3.3 to maintain chromatin integrity. Mol Cell *44*, 928–941. https://doi.org/10.1016/j.molcel.2011.12.006.

57. Strong, I.J.T., Lei, X., Chen, F., Yuan, K., and O'Farrell, P.H. (2020). Interphase-arrested Drosophila embryos activate zygotic gene expression and initiate mid-blastula transition events at a low nuclear-cytoplasmic ratio. PLOS Biology *18*, e3000891. https://doi.org/10.1371/journal.pbio.3000891.

58. Fukushima, H.S., Ikeda, T., Ikeda, S., and Takeda, H. (2024). Cell cycle length governs heterochromatin reprogramming during early development in non-mammalian vertebrates. EMBO reports, 1–24. https://doi.org/10.1038/s44319-024-00188-5.

59. Chang, F.T.M., Chan, F.L., R. McGhie, J.D., Udugama, M., Mayne, L., Collas, P., Mann, J.R., and Wong, L.H. (2015). CHK1-driven histone H3.3 serine 31 phosphorylation is important for chromatin maintenance and cell survival in human ALT cancer cells. Nucleic Acids Res *43*, 2603–2614. https://doi.org/10.1093/nar/gkv104.

60. Gratz, S.J., Ukken, F.P., Rubinstein, C.D., Thiede, G., Donohue, L.K., Cummings, A.M., and O'Connor-Giles, K.M. (2014). Highly specific and efficient CRISPR/Cas9-catalyzed homology-directed repair in Drosophila. Genetics *196*, 961–971. https://doi.org/10.1534/genetics.113.160713.

61. Berg, S., Kutra, D., Kroeger, T., Straehle, C.N., Kausler, B.X., Haubold, C., Schiegg, M., Ales, J., Beier, T., Rudy, M., et al. (2019). ilastik: interactive machine learning for (bio)image analysis. Nat Methods *16*, 1226–1232. https://doi.org/10.1038/s41592-019-0582-9.